

# 3D RECONSTRUCTION OF PLANT ROOTS FROM MRI IMAGES

Hannes Schulz<sup>1</sup>, Johannes A. Postma<sup>2</sup>, Dagmar van Dusschoten<sup>2</sup>, Hanno Scharr<sup>2</sup> and Sven Behnke<sup>1</sup>

<sup>1</sup>Computer Science VI, Autonomous Intelligent Systems, University Bonn, Friedrich-Ebert-Allee 144, 53113 Bonn, Germany

<sup>2</sup>IBG-2, Plant Sciences, Forschungszentrum Jülich, 52425 Jülich, Germany

Keywords: Root Modeling, Plant Phenotyping, Roots in Soil, Maize, Barley.

Abstract: We present a novel method for deriving a structural model of a plant root system from 3D Magnetic Resonance Imaging (MRI) data of soil grown plants. The structural model allows calculation of physiologically relevant parameters. Roughly speaking, MRI images show local water content of the investigated sample. The small, local amounts of water in roots require a relatively high resolution, which results in low SNR images. However, the spatial resolution of the MRI images remains coarse relative to the diameter of typical fine roots, causing many gaps in the visible root system. To reconstruct the root structure, we propose a three step approach: 1) detect tubular structures, 2) connect all pixels to the base of the root using Dijkstra's algorithm, and 3) prune the tree using two signal strength related thresholds. Dijkstra's algorithm determines the shortest path of each voxel to the base of the plant root, weighing the Euclidean distance measure by a multi-scale vesselness measure. As a result, paths running within good root candidates are preferred over paths in bare soil. We test this method using both virtually generated MRI images of Maize and real MRI images of Barley roots. In experiments on synthetic data, we show limitations of our algorithm with regard to resolution and noise levels. In addition we show how to use our reconstruction for root phenotyping on real MRI data of Barley roots in soil.

## 1 INTRODUCTION

In this paper, we present a method for deriving a structural model of plant roots from MRI measurements of roots in soil (cmp. Fig. 1). From this model, we then derive local root mass and diameter together with suitable statistics.

Plant roots are 'the hidden half' of plants (Waisel et al., 2002) because non-invasive root imaging in natural soils is hampered by a wide range of constrictions. For a full, non-destructive 3D assessment of root structure, topology and growth, only two main techniques are currently available, Computer Tomography, using X-Rays or neutron (Nakanishi et al., 2003; Pierret et al., 2003; Ferreira et al., 2010) and Nuclear Magnetic Resonance Imaging (MRI) (Brown et al., 1990; Southon and Jones, 1992; Jahnke et al., 2009). Both X-ray CT and MRI are volumetric 3D imaging techniques, where CT is based on absorption and MRI is an emission-based technique.

For MRI, most signal stems from water in the roots and to a lesser extend from soil water. Even though MRI contrast can be adapted such that discrimination between root water and soil water is maximized (see Sec. 3), signal-to-noise ratio (SNR) remains relatively low. In addition, contrast can be enhanced by manip-



Figure 1: A simulated maize root MRI image at SNR 150 (left) and its true and fitted structure model overlaid, with missing/additional pieces marked in strong red/blue (right).

ulating the soil mixture such that mainly signal from the roots is detected.

With the same equipment, MRI measurements can be done at different spatial resolutions, where lower resolution results in a significant reduction in measurement time. This is relevant for root phenotyping studies, where larger quantities of plants need to be measured repeatedly over a longer period. Thus, one of our main concerns is in how far a diminishing resolution and low SNR reduces the accuracy of a root reconstruction algorithm. For plant root studies, this algorithm should produce from the MRI measurements estimates for local and overall root mass, root length, and diameter. Here, we examine the capability of a novel root reconstruction algorithm to obtain these estimates at different image resolutions and noise levels.

As root diameters may be of subvoxel size, voxel-wise segmentation would be brittle. We therefore reconstruct a structural, i. e. zero-diameter model of the root system and subsequently derive parameters like local root mass and diameter, without finding step edges in the data. To construct the root structure, we first find tubular structures on multiple scales. We then determine the plant shoot position and connect every root candidate element to it by a shortest path algorithm. Finally, we prune the graph using two intuitive thresholds, and adjust node positions with subvoxel accuracy by a mean-shift procedure. For root mass and diameter estimation, we use the scale value  $\sigma$  giving maximum response of the (Frangi et al., 1998) tubularness measure  $\mathcal{V}(\sigma)$  (see Eq. 1). Root mass can then be derived by locally summing image intensities within a cylinder of the found diameter around the root center.

After reviewing related work, we start by giving a short overview of the MRI method applied (Sec. 3), followed by a description of the novel root reconstruction algorithm (Sec. 4) and how to use the reconstructed root to derive root statistics (Sec. 5). Experiments in Sec. 6 demonstrate the performance of our approach.

## 2 RELATED WORK

Data similar to ours has been analyzed extensively in the biomedical literature, e.g. using the multi-scale “vesselness” measure of (Frangi et al., 1998). Of many suggested approaches for finding and detecting vessels, (Lo et al., 2010) is most similar to ours. Our approach is less heuristic, however, and uses knowledge of global connectedness. While the primary focus of most approaches is visualization, we aim at fully automated extraction of root statistics, such as length and water distribution, to model roots and biological processes of roots.

So far, only few image processing tools are available for plant root system analysis (Dowdy et al., 1998; Mühlich et al., 2008; Armengaud et al., 2009). For these tools, however, roots need to be well visible, e. g. by invasively digging them out, washing, and scanning them or by cultivating plants in transparent agar (Nagel et al., 2006). Analysis is restricted to 2D data. Large root gaps, artifacts due to low SNR, or reconstruction in 3D have not yet been addressed.

Classical, non-invasive image-based root system analysis tools in biological studies are e. g. 2D rhizotrons (Pierret et al., 2003). 3D MRI has already been used in root-soil-systems for the analysis of e. g. water-flow (Haber-Pohlmeier et al., 2009). Semi-automated reconstruction of roots by 3D CT based on a multivariate grey-scale analysis has recently been shown to work (Tracy et al., 2010). However, to the best of the authors knowledge, fully automatic root system reconstruction in 3D data is new.

## 3 IMAGING ROOTS IN SOIL BY MRI

MRI is an imaging technique well-known from medical imaging and general background information is available in textbooks, see e. g. (Haacke et al., 1999). The MRI signal is proportional to the proton density per unit volume, modulated by an NMR relaxation phenomenon called  $T_2$  relaxation. It causes an exponential signal decrease after excitation that can be partially refocused into an echo. Plant root analysis in soil was so far hampered by a relatively poor contrast between roots and surrounding soil water. However, soil water contribution to the echo signal can be reduced to less than 1%, increasing contrast significantly. This is achieved by mixing small soil particles (a loamy sand) and larger ones and keeping the water saturation of the soil at moderate levels. Thus, the soil water  $T_2$  (relaxation time) is only a few milliseconds whereas the root water  $T_2$  is several tens of milliseconds. Using an echo time of 9 ms, the signal amplitude of soil water is damped severely, whereas the root water signal intensity is only mildly affected. Additionally, as magnetic particles disturb MRI signals heavily, such particles should be removed from the soil beforehand to assure a high-fidelity 3D image reconstruction.

The MRI experiments were carried out on a vertical 4.7 Tesla spectrometer equipped with 300 mT/m gradients and a 100 mm r.f. coil (Varian, USA). 3D images were generated using a so-called single echo multi slice (SEMS) sequence, with a field of view of 100 mm and a slice thickness of 1 mm. A barley plant was grown in a 420 mm long 90 mm diameter

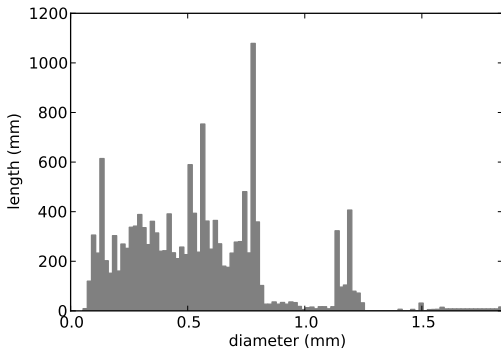


Figure 2: Root diameter distribution of the root shown in Figure 1.

PVC tube with a perforated bottom to prevent water clogging. Measurements were performed about 6 weeks after germination. Because the tube is longer than the homogeneous r.f. field, it was measured in five stages. The resulting image stacks were stitched together without any further corrections. The final  $192 \times 192 \times 410$  volumetric image has a lateral spatial resolution of 0.5 mm and a vertical resolution of 1 mm.

### 3.1 Synthetic MRI Images

Synthetic MRI images were generated using *SimRoot*, a functional-structural model capable of simulating the architecture of plant roots (Postma and Lynch, 2011a; Postma and Lynch, 2011b). Virtual root models of 15 day old maize plants<sup>1</sup> were converted into scalar valued images in which the pixel value corresponds to the root mass within the 0.5 mm cubed pixels. Five images were generated from five runs, which only varied due to variation in the model's random number generators. We added variable amounts of Gaussian noise to the images at SNRs of 10, 50, 100, 150, 200, and 500. Note that even images with high SNR cannot simply be thresholded, since roots thinner than a voxel would not be detected anymore. The resolution of the images with SNR of 150, i. e. an achievable SNR in real MRI data, were scaled down in the two horizontal dimension to voxel dimensions of 0.5, 0.67, 1, and 1.3 mm to see how the resolution of the MRI image might affect the results. Figure 1, left, shows one of the simulated maize root images, and Figure 2 its root diameter distribution. Please note, that as for real roots not all diameters are populated in the histogram.

<sup>1</sup>Barley plants are not yet available in *SimRoot*. 15 day old maize roots come closest to the barley root data.

## 4 RECONSTRUCTION OF ROOT STRUCTURE

We build a structural root model from volumetric MRI measurements in four main steps. First, we find tubular structures on multiple scales. Secondly, we determine the shoot position (the horizontal position of the plant at ground level). Thirdly, we use a shortest path algorithm to determine connectivity. Finally, we prune the graph using two intuitive thresholds.

**Finding Tubular Structures.** We follow the approach proposed by (Frangi et al., 1998), which is widely used in practice. MRI images typically do not contain isotropic voxels. The axes are therefore first scaled up using cubic spline interpolation. The result  $L(\mathbf{x})$  (Fig. 3(b)) is then convolved with a three-dimensional isotropic derivative of a Gaussian filter  $G(\mathbf{x}, \sigma)$ . The standard deviation  $\sigma$  determines the scale of the tubes we are interested in:

$$\frac{\partial}{\partial x} L(\mathbf{x}, \sigma) = \sigma^\gamma L(\mathbf{x}) * \frac{\partial}{\partial x} G(\mathbf{x}, \sigma).$$

In the factor  $\sigma^\gamma$ , introduced by (Lindeberg, 1996) for fair comparison of scales,  $\gamma$  is set to 0.78 (for a tubular root model as in (Krissian et al., 1998)). Differentiating again yields the Hessian matrix  $H_o(\sigma)$  for each point  $\mathbf{x}_o$  of the image. The local second-order structure captures contrast between inside and outside of tubes at scale  $\sigma$  as well as the tube direction. Let  $\lambda_1, \lambda_2, \lambda_3$  ( $|\lambda_1| \leq |\lambda_2| \leq |\lambda_3|$ ) be the eigenvalues of  $H_o(\sigma)$ . For tubular structures in  $L$  holds:  $|\lambda_1| \approx 0$ ,  $|\lambda_1| \ll |\lambda_2|$ , and  $|\lambda_2| \approx |\lambda_3|$ . The signs and magnitudes of all three eigenvalues are combined in the medialness measure  $\mathcal{V}'_o(\sigma)$  proposed in (Frangi et al., 1998) (Fig. 3(c)), determining how similar the local structure at  $\mathbf{x}_o$  is to a tube at scale  $\sigma$ :

$$\mathcal{V}'_o(\sigma) = \begin{cases} 0 & \text{if } \lambda_2 > 0 \text{ or } \lambda_3 > 0 \\ \underbrace{\left(1 - e^{-\frac{\lambda_3^2}{2\alpha^2\lambda_2^2}}\right)}_{\mathcal{R}_A} \underbrace{e^{-\frac{\lambda_1^2}{2\beta^2|\lambda_2\lambda_3|}}}_{\mathcal{R}_B} \underbrace{\left(1 - e^{-\frac{\sum_i \lambda_i^2}{2c^2}}\right)}_S & \end{cases}.$$

Here,  $\mathcal{R}_A$  distinguishes between plate-like and line-like structures,  $\mathcal{R}_B$  is a measure of how similar the local structure is to a blob, and  $S$  is larger in regions with more contrast. The relative weight of these terms is controlled by the parameters  $\alpha$  and  $\beta$ , which we both fixed at 0.5. Finally, we combine the responses of multiple scales by selecting the maximum response

$$\mathcal{V}'_o = \max_{\sigma \in \{\sigma_0, \dots, \sigma_S\}} \mathcal{V}'_o(\sigma). \quad (1)$$

where  $\sigma_i = (\sigma_S/\sigma_0)^{i/S} \cdot \sigma_0$ . For our experiments, we select  $\sigma_0 = 0.04$  mm,  $\sigma_S = 1.25$  mm, and  $S = 20$ .

**Finding the Shoot Position.** In our model, we utilize the fact that plant roots have a tree graph structure. The root node of this tree is a point at the base of the plant shoot, which has, due to its high water content and large diameter, a high intensity in the image. To determine the position of the base of the plant shoot  $\mathbf{x}_r$ , we find the maximum in the ground plane slice  $p$  convolved with a Gaussian  $G(\mathbf{x}, \sigma)$  with large  $\sigma$ ,

$$\mathbf{x}_r = \arg \max_{\mathbf{x}} \{L(\mathbf{x}, \sigma) | x_3 = p\}.$$

**Determining Connectivity.** So far, we have a local measure of vesselness  $\mathcal{V}$  at each voxel and an initial root position  $\mathbf{x}_r$ . What is lacking, is whether two neighboring voxels are part of the same root segment and how root segments are connected. In contrast to some medical applications, we can use the knowledge of global tree connectedness. For this purpose, we first define a graph on the voxel grid, where the vertices are the voxel centers and edges are inserted between all voxels in a 26-neighborhood. We further define an edge cost  $w$  for an edge between  $\mathbf{x}_s$  and  $\mathbf{x}_t$  as

$$w(\mathbf{x}_s, \mathbf{x}_t) = \exp(-\omega(\mathcal{V}_s + \mathcal{V}_t))$$

with  $\omega \gg 0$ . For each voxel  $\mathbf{x}_o$ , we search for the minimum-cost path to  $\mathbf{x}_r$ . This can efficiently be done using the Dijkstra algorithm (Dijkstra, 1959), which yields a predecessor for each node in the voxel graph, determining the connectivity.

**Model Construction.** Every voxel  $\mathbf{x}_o$  is now connected to  $\mathbf{x}_r$ , but we already know that not all voxels are part of the root structure. The voxel graph needs to be pruned to represent only the roots. For this purpose, it is sufficient to select leaf node candidates that exceed the two thresholds explained below. The nodes and edges on the path from leaf node  $\mathbf{x}_l$  to  $\mathbf{x}_r$  in the voxel graph are then added to the root graph.

In a first step we cut away all voxels from the graph with  $L(\mathbf{x}) < L_{\min}$ , meaning that a leaf node candidate needs to contain a minimum amount of water.

In a second step, we find leaf nodes of the tree, i. e. root tips. To do so, we search for high values in a median-based ‘upstream/downstream ratio’  $D$  for voxel  $\mathbf{x}_o$

$$D_o = \text{median}_{\mathbf{u} \in N_m^+(\mathbf{x}_o)}(L(\mathbf{u})) / \text{median}_{\mathbf{d} \in N_m^-(\mathbf{x}_o)}(L(\mathbf{d})),$$

where neighborhood  $N_m^-(\mathbf{x}_o)$  denotes the  $m$  predecessor voxels of  $\mathbf{x}_o$  with highest  $\mathcal{V}$  when following the graph for  $m$  steps away from  $\mathbf{x}_r$  (i. e. into the soil), and  $N_m^+(\mathbf{x}_o)$  are the  $m$  successor voxels with highest  $\mathcal{V}$  when following the graph for  $m$  steps towards  $\mathbf{x}_r$  (i. e. into the root). Thus,  $D_o$  is approx. 1 for voxels surrounded by soil and voxels lying in a root since

there, the only variations of  $L(\mathbf{x})$  are due to noise.  $D_o$  is largest and in the range of SNR for voxels indicating a root tip as we encounter ‘signal’ on the one side of the voxel and ‘noise’ on the other. Thus root tips are voxels where  $D_o > D_{\min}$ , where  $D_{\min}$  is a tuning parameter.

In roots with large diameter, there are still multiple paths from the outer rim to the root center. In a final step, we remove segments which contain a leaf and are shorter than the maximum root radius from the root graph. This step is iterated as long as segments can be removed from the graph.

## 5 ESTIMATION OF ROOT PARAMETERS

In most biological contexts local and global parameters describing the phenotype of a root are needed, e. g. to derive species-specific models of roots. In this section, we show how to derive such parameters supported by our model.

**Root Lengths.** To determine the root lengths, high-precision positioning of vertices is essential. So far, vertices are positioned at voxel centers. We now apply a mean-shift procedure to move the nodes to the center of the root with subvoxel precision. At each node  $n$  at position  $\mathbf{x}_n$ , we estimate the inertia tensor in a radius of 3 mm and determine its eigenvalues  $\lambda_1 \leq \lambda_2 \leq \lambda_3$  as well as corresponding eigenvectors  $\mathbf{v}_1, \mathbf{v}_2, \mathbf{v}_3$ . If  $\lambda_3 > 1.5\lambda_2$ , we assume  $\mathbf{v}_3$  to correspond to the local root direction. We then move the node to the mean of a neighborhood in the voxel grid weighted by the vesselness measure  $\mathcal{V}$  (Eq. 1). To do so, we choose a 4-neighborhood of  $\mathbf{x}_n$  in the plane spanned by  $\mathbf{v}_1$  and  $\mathbf{v}_2$ , and evaluate  $\mathcal{V}$  by linear interpolation. Nodes where no main principal axis can be determined ( $\lambda_3 < 1.5\lambda_2$ ) are moved to the mean of their immediate neighbors in the root graph. We iterate these steps until convergence. The resulting structural model is shown in Fig. 3(a). Finally, we can determine the total root lengths by summing over all edge lengths.

**Root Radius.** For estimation of the local root radius  $r(\mathbf{x})$ , we use the argument leading to the maximum response  $\mathcal{V}_o$  in Eq. 1

$$r_o = \arg \max_{\sigma \in \{\sigma_0, \dots, \sigma_5\}} \mathcal{V}_o(\sigma) \quad (2)$$

at location  $\mathbf{x}_o$ . The radius assigned to a node is calculated by averaging  $r$  in each segment. A root segment is a list of all vertices connected to each other by exactly two connections, meaning they are either ended by a junction or a root tip.



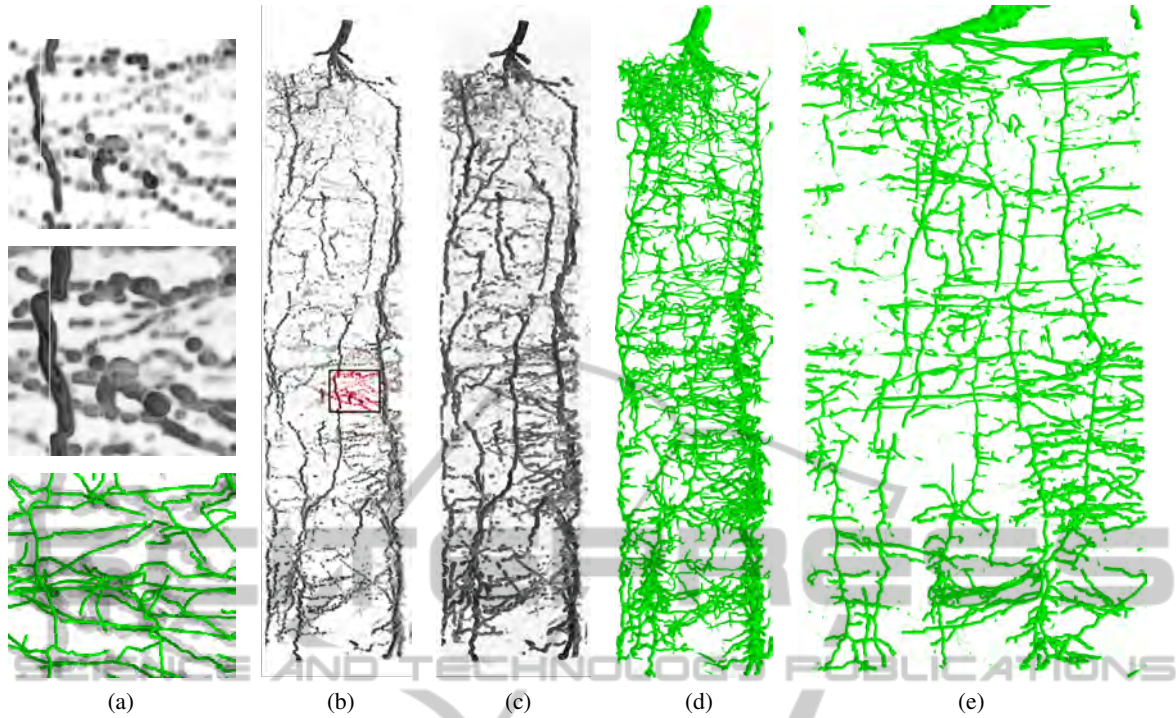


Figure 3: Root model reconstruction. (a) Raw data, tubeness-measure (Frangi et al., 1998), structural model. Volume rendering of (b) raw data and (c) tubeness-measure. (d) 3D rendering of model, edges weighted by estimated diameter. (e) Cylindrical projection of model.

**Root Mass.** Root mass is derived by sampling along segments in 0.2 mm steps. We mark for each sampling location  $\mathbf{x}_o$  all voxels within the local radius  $r_o$ . The mass of a root segment is the sum of values  $L$  of all marked voxels.

For constant water density  $\rho$  in the roots the mass of a root slice of length  $l$  can be calculated from its radius and vice versa

$$m_o = \rho \pi r_o^2 l \quad (3)$$

Thus especially for subvoxel roots mass estimate may be used as a radius measure.

## 6 EXPERIMENTS

### 6.1 Synthetic Maize Roots

Of the five synthetic root systems, one root system is set aside to tune the two thresholding parameters from Sec. 4 so that they maximize the  $F_{0.5}$  measure (van Rijsbergen, 1979)

$$F_{0.5} = \frac{1.25P \cdot R}{0.25P + R} \quad (4)$$

with precision  $P$  and recall  $R$ . Precision  $P$  is the fraction of true positives in all found positives (true and false positives), while recall is the fraction of true positives in all elements that should have been found (true positives and false negatives). The precision  $P$  has double the weight of recall  $R$  in the  $F_{0.5}$  measure in order to reduce the chance of false positives. As a result the chance of false negatives increases, however this error is relatively small compared to the current detection error of fine roots by the MRI.

To determine true/false positives and false negatives for precision and recall, we sample synthetic and reconstructed roots in 0.2 mm steps and determine the closest edge of the respective other model. A ‘match’ occurs when this distance is smaller than one voxel size.

### 6.2 Sensitivity to Resolution and Noise

For quantitative analysis of our reconstruction algorithm, we use synthetic data of maize roots (see Sec. 3). Fig. 4 shows a typical detail view of such data at SNR 150. At this SNR Frangi’s tubularness measure (Eq. (1), Fig. 4b) gives a reasonable indication of where the root is. Figs. 4c, d show the found positions before and after subvoxel positioning. In Fig. 4d we

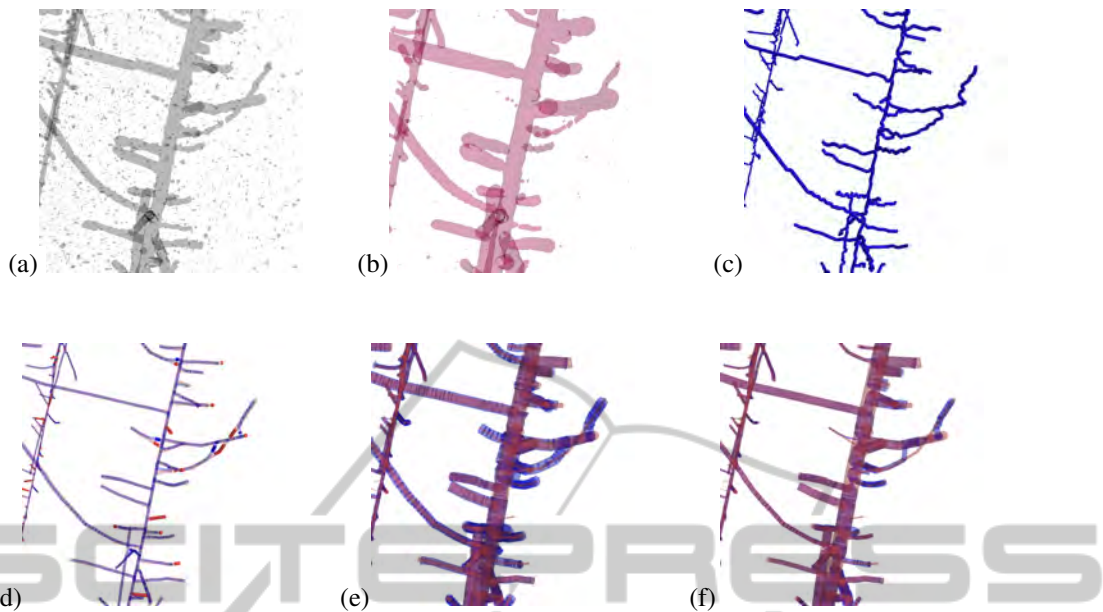


Figure 4: Example of a reconstructed root (detail): false positives, false negatives, and diameter estimates. (a) Raw data at SNR 150, (b) tubular structures enhanced using Eqn. (1), (c) extracted structure model before subvoxel positioning, (d) true and fitted structure model overlaid, with missing/additional pieces marked in strong red/blue, (e) diameter estimates, (f) mass estimates.

see that most parts of the root system are correctly detected, however, at junctions and crossings the algorithm sometimes prefers shortcuts over the true root path. For root length the effect has not much influence, however branching angles are slightly biased towards  $90^\circ$ . In addition, as short ( $< 3$  mm) root elements are suppressed for the sake of robustness with respect to noise and uncorrect skeletonization of thick roots, true short root elements are non-surprisingly missing.

Diameter and mass of the roots are shown in Fig. 4e, f, where in Fig. 4e diameter is estimated from the Frangi scales (Eq. 2), and in Fig. 4f diameter is calculated from the estimated mass (by inverting Eq. 3). We observe that radius from mass, i. e. from the measured image intensities, is much more reliable than the geometry-based estimate—especially for smaller roots. However, this is only possible under the assumption of constant water density in the root, being perfectly true for our synthetic data. While for healthy roots this is also well fulfilled, the radius of drying roots will unavoidably be systematically underestimated by this method.

In the next sections we investigate the statistical properties of the found root systems with respect to root length, volume, and diameter.

### 6.2.1 Root Length

Data acquisition time for MRI scales with image reso-

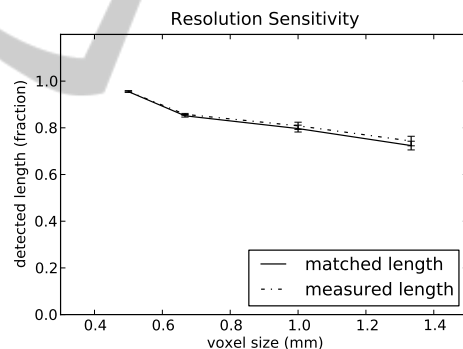


Figure 5: Influence of image resolution: fraction of detected overall root length versus voxel size, for five individual data sets showing 15 day old maize roots at SNR 150. Matched length indicates true positives only, measured length also includes false positives.

lution. Therefore, image resolution should be selected as low as possible with respect to the measurement task at hand. In order to test sensitivity of our root reconstruction algorithm with respect to image resolution, we calculated root length from the synthetic MRI data (see Sec. 3) with  $\text{SNR} = 150$  and varying image resolution and compared to the known ground truth. Fig. 5 shows how detected root length decreases with larger voxel sizes. For the highest resolution provided (0.5 mm), 95.5% of the true overall root length is detected with standard deviation 0.3%, which is well acceptable for most plant physiological studies.

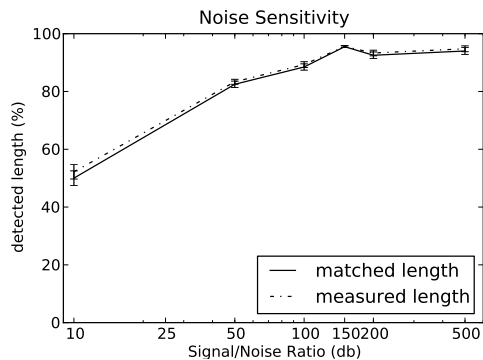


Figure 6: Influence of noise: fraction of detected overall root length versus signal to noise ratio, for five individual data sets showing 15 day old maize roots at 0.5 mm voxel size. Matched length indicates true positives only, measured length also includes false positives.

Increasing voxel size quickly decreases found root length to 80% at 1 mm voxel size and to  $\approx 72\%$  at 1.33 mm voxel size. For larger voxels, false positives have a measurable influence of about 2%. For high-resolutions, false positives have no significant influence. We conclude, that voxel size should not be greater than 0.5 mm.

As with other imaging modes, SNR of MRI data increases with acquisition time. Thus, to keep acquisition time short, image noise should be selected as high as possible with respect to the measurement task at hand. We calculated root length from the synthetic MRI data (see Sec. 3) with 0.5 mm voxel size and varying noise levels and compared to the known ground truth (see Fig. 6). For the lowest SNR (10), only 50% of the roots are detected. Detection rate quickly increases with increasing SNR and levels off to 95% at an SNR of about 150. At the given resolution, an SNR of 150–200 seems to give the best balance between detection accuracy and measuring time.

### 6.2.2 Root Mass and Diameter

Root biologists commonly divide the root system into diameter classes. The derived root diameter distribution and the corresponding volume and mass distributions give insight in the soil exploration strategy of the plant. In Fig. 7, we show scatter plots (i. e. 2D histograms) for true versus measured diameter and volume for SNR 500, 150, and 50. The drawn slope 1 line indicates perfect matches. In the high SNR case (Fig. 7a) diameters between approx. 1 and 1.6 voxels (0.5 mm to 0.8 mm) are reliably measured. Diameters between 0.5 and 1 voxel are slightly overestimated and smaller diameters are strongly biased towards 1 voxel (0.5 mm) diameter. For diameters larger than 1.6 voxels much less root elements are available (cmp. Fig. 2),

thus the shown scatter plots are less populated there. We observe however, that diameters are slightly overestimated there. Comparing Figs. 7a and 7b shows that for roots thicker than 1 voxel diameter estimates do not significantly change when increasing noise from SNR 500 to SNR 150. Subvoxel diameters are more strongly biased towards 1 voxel, meaning that such roots are still found reliably but their diameter cannot be estimated accurately. For SNR 50 overestimation becomes even stronger and is also well visible for diameters up to approx. 0.75 mm. Root mass estimates and diameters derived from them are much more robust (see Fig. 8). For SNR 500 and 150 almost no difference is visible, while for SNR 50 results are slightly worse, but still much better than the ones derived via the Frangi scale  $\sigma$ , even at SNR 500.

## 6.3 Real MRI Measurements

We calculate statistical properties of barley roots in order to demonstrate the usefulness of our algorithm on real MRI images of roots. Obviously, there are a wealth of possibilities of how statistics on the modeled root system may be built. In the following, we give two examples where

1. the plausibility of the results can easily be checked visually,
2. results cannot be achieved from the MRI images directly, and
3. structural information on the roots is needed.

**Length Distribution between Furcations.** This measure cannot be derived from local root information, as connectedness between furcations needs to be ensured. We define a *segment* as list of connected edges  $\{e_i(n_i, n_{i+1})\}$ ,  $i \in \{0, \dots, N\}$  where all intermediate nodes  $n_k$ ,  $k \in 1, \dots, N-1$  have  $\text{indegree}(n_k) = 1$  and  $\text{outdegree}(n_k) = 1$ . A segment is horizontal/vertical if the vector  $n_N - n_0$  draws an angle smaller than  $45^\circ$  with the horizontal/vertical axis. Here, we find that horizontal segments have an average length of  $8.8 \pm 7.77$  mm, whereas vertical segments have an average length of  $5.10 \pm 5.20$  mm. Segments containing a root tip are excluded in this average. We conclude, that vertical roots have greater branching frequency than the horizontal (higher order) roots.

**Distribution of Mass.** The MRI voxel grid allows to calculate the total mass of a plant. Using the model constructed above, this mass distribution can now be analyzed in new ways, which may be useful when building statistical models of root growth. In Fig. 9, we show the distribution of mass under the model (as



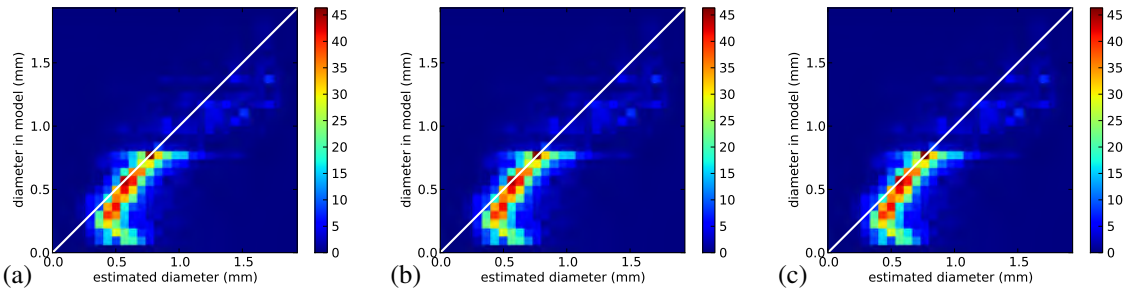


Figure 7: Histograms of true versus measured diameter at resolution 0.5 mm and (a) SNR 500, (b) SNR 150, and (b) SNR 50. Diameter was measured using Eq. 2. For matching, each root was sampled in 0.2 mm steps and counted as “matched” if a corresponding line segment in the other root was closer than one voxel size.

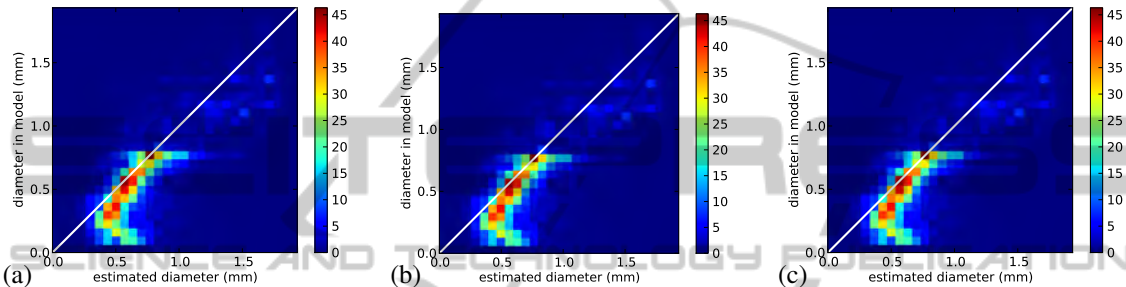


Figure 8: Same as Fig. 7, however with diameter estimated from local mass (cmp. end of Sec. 5).

derived in Sec. 5) as a function of the depth and the root angle. We distinguish between expected mass of a root at a certain depth/angle and the total mass at this point. The data clearly shows that horizontal roots bind most water (left), while vertical roots are less abundant, but are expected to be heavier (middle). These results agree with current biological understanding of the root architecture of barley plants, which is characterized by a small number of thick, vertically growing nodal roots and a large number of fine horizontally growing lateral roots, branching off the nodal roots.

#### 6.4 Algorithm Runtime

On the  $192 \times 192 \times 410$  reference dataset, a complete, partially parallelized run currently takes less than 20 minutes on a  $12 \times 2.67$  GHz core Intel machine. For the sake of algorithmic simplicity, the dataset currently needs to provide cubic voxels. Thus, the coarse vertical direction is upsampled resulting in a doubling of the number of voxels. Avoiding this and using the speed up potential through further parallelization of the Hessian computation (across multiple computers) and later steps (across multiple cores) may reduce the computation time significantly.

## 7 SUMMARY AND CONCLUSIONS

In this paper, we showed how to derive a structural model of root systems from 3D MRI measurements and assign mass and radius to found root segments.

From our experiments on the dependence of found root length on image resolution and SNR, we conclude that root system reconstruction strongly depends on resolution, with better detection rates at higher resolution. This is in coherence with the naïve expectation. Also sensitivity to noise is as expected. SNR below 100 severely effects detection accuracy of roots with subvoxel diameters. Systematical errors of the derived root structure occur at junctions, where branching angles are biased towards  $90^\circ$ . A closer analysis of junctions should therefore be investigated in future research. However other measures are already well applicable. Especially mass estimation (and radius estimation when water density in roots is constant) turned out to be robust against SNR reduction, while geometry-based diameter estimates from Frangi scales become less and less reliable. For healthy roots, radius from mass is an excellent alternative to geometry-based measures, but in drying roots water density is nonconstant and more sophisticated radius measurements should be investigated.



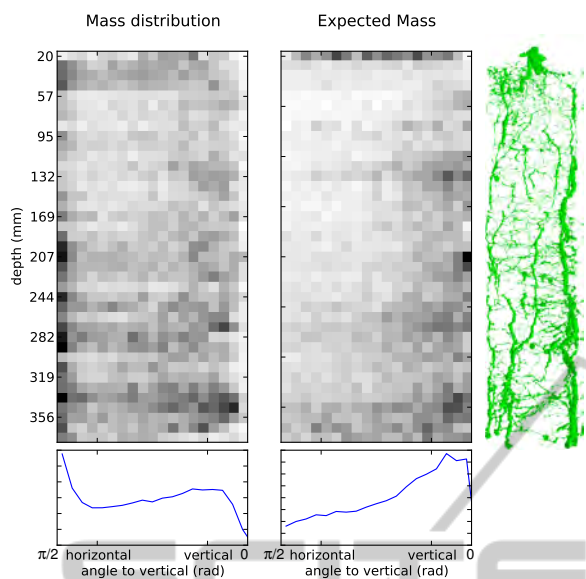


Figure 9: Mass distribution in root, w.r.t. depth and root angle. Darker regions represent more mass. Left: Unnormalized mass, shows that horizontal roots are prevalent and bind most of the water. Middle: Mass normalized by number of roots, shows that vertical roots tend to have more mass than horizontal ones. Directly beneath the soil surface, roots tend to have more mass regardless of direction. Bottom plots depict the marginal mass distribution of angle. Right: Model visualization weighted by estimated mass (cmp. Fig. 3).

For real data of barley roots we showed, how the derived structural and local quantities can readily be used for plant root phenotyping.

## REFERENCES

- Armengaud, P., Zambaux, K., Hills, A., Sulpice, R., Patison, R. J., Blatt, M. R., and Amtmann, A. (2009). Ez-rhizo: integrated software for the fast and accurate measurement of root system architecture. *Plant Journal*, 57(5):945–956.
- Brown, J. M., Kramer, P. J., Cofer, G. P., and Johnson, G. A. (1990). Use of nuclear-magnetic resonance microscopy for noninvasive observations of root-soil water relations. *Theoretical and Applied Climatology*, pages 229–236.
- Dijkstra, E. (1959). A note on two problems in connexion with graphs. *Numerische Mathematik*, 1(1):269–271.
- Dowdy, R., Smucker, A., Dolan, M., and Ferguson, J. (1998). Automated image analyses for separating plant roots from soil debris elutriated from soil cores. *Plant and Soil*, 200:91–94.
- Ferreira, S., Senning, M., Sonnewald, S., Kefling, P.-M., Goldstein, R., and Sonnewald, U. (2010). Comparative transcriptome analysis coupled to x-ray ct reveals sucrose supply and growth velocity as major determinants of potato tuber starch biosynthesis. *BMC Genomics. Online journal*, 11(17).
- Frangi, A., Niessen, W., Vincken, K., and Viergever, M. (1998). Multiscale vessel enhancement filtering. *Medical Image Computing and Computer-Assisted Intervention (MICCAI)*, pages 130–137.
- Haacke, E., Brown, R., Thompson, M., and Venkatesan, R. (1999). *Magnetic Resonance Imaging, Physical Principles and Sequence Design*. John Wiley & Sons.
- Haber-Pohlmeier, S., van Dusschoten, D., and Stapf, S. (2009). Waterflow visualized by tracer transport in root-soil-systems using MRI. In *Geophysical Research Abstracts*, volume 11.
- Jahnke, S., Menzel, M. I., van Dusschoten, D., Roeb, G. W., Bühler, J., Minwuyet, S., Blümmler, P., Temperton, V. M., Hombach, T., Streun, M., Beer, S., Khodaverdi, M., Ziemons, K., Coenen, H. H., and Schurr, U. (2009). Combined MRI-PET dissects dynamic changes in plant structures and functions. *Plant Journal*, pages 634–644.
- Krissian, K., Malandain, G., Ayache, N., Vaillant, R., and Trousslet, Y. (1998). Model based multiscale detection of 3d vessels. In *Proceedings of the Workshop on Biomedical Image Analysis*, pages 202–210. IEEE.
- Lindeberg, T. (1996). Edge detection and ridge detection with automatic scale selection. In *CVPR*, pages 465–470.
- Lo, P., van Ginneken, B., and de Bruijne, M. (2010). Vessel tree extraction using locally optimal paths. In *Biomedical Imaging: From Nano to Macro*, pages 680–683.
- Mühlich, M., Truhn, D., Nagel, K., Walter, A., Scharf, H., and Aach, T. (2008). Measuring plant root growth. In *Pattern Recognition 2008*, volume 5096 of *Lecture Notes in Computer Science*, pages 497–506. Springer.
- Nagel, K. A., Schurr, U., and Walter, A. (2006). Dynamics of root growth stimulation in nicotiana tabacum in increasing light intensity. *Plant Cell and Environment*, 29(10):1936–1945.
- Nakanishi, T., Okuni, Y., Furukawa, J., Tanoi, K., Yokota, H., Ikeue, N., Matsubayashi, M., Uchida, H., and Tsiji, A. (2003). Water movement in a plant sample by neutron beam analysis as well as positron emission tracer imaging system. *Journal of Radioanalytical and Nuclear Chemistry*, 255:149–153.
- Pierret, A., Doussan, C., Garrigues, E., and Kirby, J. M. (2003). Observing plant roots in their environment: current imaging options and specific contribution of two-dimensional approaches. *Agronomy for Sustainable Development*, 23(5–6):471–479.
- Postma, J. A. and Lynch, J. P. (2011a). Root cortical aerenchyma enhances the acquisition and utilization of nitrogen, phosphorus, and potassium in ze mays I. *Plant Physiology*, 156(3):1190–1201.
- Postma, J. A. and Lynch, J. P. (2011b). Theoretical evidence for the functional benefit of root cortical aerenchyma in soils with low phosphorus availability. *Annals of Botany*, 107(5):829–841.
- Southon, T. E. and Jones, R. A. (1992). NMR imaging of roots – methods for reducing the soil signal and for obtaining a 3-dimensional description of the roots. *Physiologia Plantarum*, pages 322–328.

- Tracy, S., Roberts, J., Black, C., McNeill, A., Davidson, R., and Mooney, S. (2010). The X-factor: visualizing undisturbed root architecture in soils using X-ray computed tomography. *Journal of Experimental Botany*, 61(2):311–313.
- van Rijsbergen, C. (1979). *Information Retrieval*. Butterworth, London, Boston, 2nd edition.
- Waisel, Y., Eshel, A., and Kafkafi, U., editors (2002). *Plant Roots: The Hidden Half*. Marcel Dekker, Inc.

